ACS OMEGA

Open Access

This article is licensed under CC-BY-NC-ND 4.0

http://pubs.acs.org/journal/acsodf

Article

Enhancing the Electrical Performance of Formamidinium Perovskites through WS_2 Nanotube Incorporation

Stjepan Dolić, Vedran Kojić,* Alla Zak, Alex Laikhtman, Hongbo Mo, Tihana Čižmar, Ina Erceg, Lucija Klobučar, Iva Šrut Šrut Rakić, Krunoslav Juraić, and Andreja Gajović

Cite This: *ACS Omega* 2026, 11, 26411−26420

Read Online

ACCESS | Metrics & More | Article Recommendations | Supporting Information

ABSTRACT: Organometal lead-halide perovskite (LHPs) thin films are on the brink of commercialization as their performance reaches that of silicon solar cells. As organometal lead-halide perovskite films are solution-processed, they are particularly suitable for the preparation of composite films with other semiconductor materials, which can improve the electronic properties of the films. In this work, WS_2 hollow nanotubes, synthesized using a high-temperature vapor-gas−solid (VGS) reaction, are dispersed inside the perovskite thin film and investigated by utilizing the capabilities of solid-state impedance spectroscopy (IS) to measure electrical conductivity. By adding an energy-level-compatible semiconducting material inside the absorber thin film, we were able to observe an increase in the conductivity of the film without diminishing optical properties, showing that WS_2 nanotubes can be used as additives in the preparation of perovskite thin films.

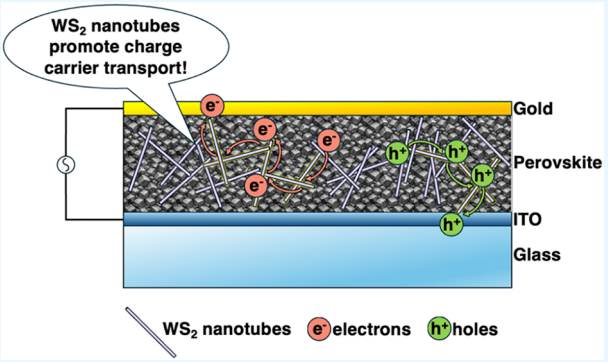

INTRODUCTION

For more than a decade, lead-halide perovskites (LHPs)[1] have attracted attention because of their high photoluminescence quantum yield as well as their scalable and versatile processability with solution-based thin-film preparations.[2] These materials can be applied in areas such as solar-cell absorber materials, light-emitting diodes, photodetectors, lasers, photocatalysis, and thermoelectrics.[3−9] LHP solar cells have certified efficiencies of up to 26.9%,[10] with outstanding parameters of 27.13 mA cm^{-2} for the short-circuit current (J_{sc}), 1.203 V for the open-circuit voltage (V_{oc}), and fill factors of up to 82.3%. However, despite the advancement of the efficiency of LHP solar cells, there are still significant problems to overcome in terms of LHP stability. In addition, other applications of LHPs can be hindered by their low conductivity, such as thermoelectrics.[8]

In general, the stability of LHPs is negatively affected by exposure to moisture,[11,12] oxygen,[13,14] illumination,[15] and elevated temperature.[16] In addition, crystal defects, common in grain boundaries of polycrystalline films, can be the source of an induced nonradiative recombination of photogenerated charge carriers.[17] These defects can, in turn, affect both the performance and stability of LHP devices. The film morphology, defect densities, and optical and electrical properties are all strongly dependent on LHP composition and the sample preparation. Consequently, there is significant interest in a better understanding of the effect of the film composition on the LHP properties. While there have been numerous studies on the structure, morphology, and the optical properties of LHPs,[18−21] as well as effects of device fabrication,[22,23] electrical measurements of LHPs are mostly focused on solar-cell J-V curves, from which the solar-cell parameters can be extracted. However, other types of electrical measurements, such as determination of charge carrier concentration and mobility in the literature, have been scarce, likely due to problems in applying common characterization techniques to LHPs.

One of the most widely used techniques is a Hall-effect measurement,[24] which can provide information on the mobility and species of the major carriers responsible for the conductivity, provided that the samples are sufficiently conductive. However, due to the low conductivity of LHPs, the Hall-effect technique cannot be used. Another possible technique to measure mobility is the space-charge-limited current (SCLC method).[25,26] While this can provide additional information, such as the trap density, it is very sensitive to the series resistance and the presence of energy barriers in the metal−semiconductor junction, which impacts the calculation of the charge carrier mobility.[27] On the other hand, impedance

Received: November 12, 2025
Revised: March 20, 2026
Accepted: April 3, 2026
Published: April 30, 2026



ACS Publications

© 2026 The Authors. Published by American Chemical Society

Downloaded from pubs.acs.org/acsodf/article-pdf/11/18/26411/6614355/4/acsomega.5c11459.pdf by guest on 24 November 2026

spectroscopy (IS)[28] is a powerful technique that can provide useful information about the electrical conductivity of the material over a wide range of frequencies. This method has been used for LHP solar-cell devices,[29,30] but it can also be used to investigate the absorber-layer electrical properties, mainly when materials are modified to improve their properties.

Different approaches have been used in the literature to improve the conductivity of LHP, such as using non-stoichiometric compositions (self-doping) or doping with substitutional dopants such as Bi.[8] However, the majority of doping investigations have been performed on $MAPbI_3$, rather than on different mixed composition perovskite films. Instead of elemental dopants, composite materials can be used to enhance the electrical conductivity. Various nanomaterials could potentially be used to achieve composite films with enhanced conductivity. However, the major challenge in preparing composite films is achieving uniform distribution of nanomaterial within the perovskite matrix and retaining favorable film quality (morphology, roughness, optical properties) while improving electrical conductivity. There have been reports of various nanomaterial incorporation into lead halide perovskite thin films, which influence their electrical properties. Several reports have shown that the inclusion of carbon nanotubes influenced the electrical conductivity of perovskite thin films, hypothesizing that carbon nanotubes induce the influence of *p*-type doping effects and enhance the electron transfer mechanism.[31,32] Noble metal nanoparticles, specifically gold, can also improve efficiency of perovskite solar cells due to localized surface plasmon resonance.[33] Lead sulfide quantum dots have shown how nanosemiconductors can also influence electrical transport properties.[34]

Among possible materials of interest for preparing LHP composites, transition-metal dichalcogenides (TMDs) stand out due to their exceptional properties. TMDs have the chemical formula MX_2, where M is a Group-VI transition metal (Cr, Mo, and W) and X is a chalcogen nonmetal (S, Se, and Te). TMD nanostructures such as nanotubes (NTs) and nanoparticles (NPs) are made of S−M−S layers stacked via van der Waals forces.[35] Among the transition-metal dichalcogenides, tungsten disulfide (WS_2) is a semiconducting material with an indirect band gap of 1.9 eV.[36] When WS_2−NTs are synthesized, they form a closed-cage structure with a low density of dangling bonds and defects.[37] Additionally, WS_2 has been shown to have a strong ability to conduct both electrons and holes as well as having a high absorption coefficient.[38−40] Thus, it is plausible to hypothesize that combining WS_2 nanostructured materials with LHP absorber layers could yield an improvement in the electrical properties of LHP thin films.

There have been several reports about including WS_2 nanomaterials inside various perovskite-structure matrices. Germanium-halide perovskites were combined with WS_2 nanoflakes to fabricate field-effect transistors.[41] Combining these two materials resulted in an increase in the external quantum efficiency and conductivity. In addition, WS_2 was combined with 2D perovskites to achieve energy up-conversion, thus boosting the efficiency of 2D-based solar-cell devices.[42] Attempts with LHP/WS_2 have also been made in recent years. WS_2 nanosheets were combined with methylammonium lead iodide (MAPI) LHPs to produce a very responsive phototransistor,[43] while claiming to improve the stability of MAPI LHPs using WS_2 NPs.[44]

In this study, we have fabricated WS_2 nanotubes and found the protocol for the dispersion of the resulting NTs inside the FA-based lead-halide perovskite absorber layer to improve its electrical conductivity. A protocol for the dispersion of NTs utilizes the mesoscopic nature of the WS_2 frame through the bulk of the FA-dominant perovskite (PVSK) layer. We used FA-dominant PVSK layers as these have been found to be more relevant in terms of performance and stability in comparison to MA-dominant perovskite layers.[45] The WS_2−NTs were synthesized by a combined sulfidation-reduction process from tungsten oxides in a high-temperature vapor-gas−solid (VGS) reaction. The obtained powder was suspended in the organic solvent from which the perovskite solution was prepared. The proposed hypothesis is that, combining two semiconducting materials, in which one component (the additive) has better electrical properties (WS_2−NTs), will lead to an improvement of the bulk material's electrical properties. The as-prepared PVSK and PVSK/WS_2−NTs composite thin films were characterized by using grazing-incidence XRD, profilometry, dynamic light scattering (DLS), transmission electron microscopy (TEM), scanning electron microscopy (SEM), UV−vis spectroscopy, and impedance spectroscopy. An improvement in the electrical conductivity was shown when incorporating an appropriate amount of WS_2−NTs, while the inclusion of WS_2−NTs in the PVSK did not impact the structure, morphology, or optical properties.

MATERIALS AND METHODS

Preparation of WS_2−NT

Tungsten disulfide (WS_2) nanotubes (NTs) were synthesized using a high-temperature, vapor-gas−solid (VGS), one-pot reaction of WO_3 with H_2/H_2S gases, where the growth of suboxide nanowhiskers precedes their sulfurization into hollow WS_2 NTs. The nanoparticles of tungsten oxide, 100 nm in diameter, were used as a precursor to produce tens-of-microns-long NTs. Such dramatic changes in the size of the precursor during this reaction require the vapor as a "building material", which became available after the initial reduction of the precursor oxide into a volatile suboxide W_4O_{11} phase. An additional partial reduction of oxide vapor into nonvolatile dioxide provokes the spontaneous, very rapid (1−2 min) crystallization of the vapor mixture into nanowhiskers of $W_{18}O_{49}$. This suboxide phase is known to be stable against reduction and has a tunneling structure that is beneficial for one-dimensional crystallization. The sulfurization started from the nanowhiskers' surface and continued inward through the slow diffusion of the reactive gases, while a few initial layers guided the growth of the next layers, serving as an epitaxial-like substrate. It is worth mentioning that all the steps of this reaction are carried out at the same reactor, at the same temperature, and in the same flow of gases, following each other in a self-controlled manner. The pure WS_2 phase was confirmed by the XRD pattern in Figure 1. The NTs obtained were 20−180 nm in diameter and 5−20 μm long, as shown in the TEM and SEM images (Figure 2).

The small shift of (001) lines to lower angles in the XRD spectrum of WS_2−NTs is a typical phenomenon for the nanoparticles and nanotubes formed from bent or rolled layers. This phenomenon can serve as a nanostructure fingerprint, confirming the formation of pure-phase, closed-cage nanotubes rather than bulk platelets, in which the layers are parallel. The position of the peak (smaller 2θ) indicates an increase, by approximately 2% approximately, in interlayer spacing of nanotubes compared to platelets (as follows from Bragg's law: $2d \sin\theta = n\lambda$). This change was attributed to lattice strain resulting from the three-atomic S−W−S rigid layers bending into nanotubes.[46,47] The nanotube diameter, calculated using the Debye−Scherrer equation, yields an average diameter of 80 nm.

Downloaded from pubs.acs.org/acsodf/article-pdf/11/18/26411/6614354/acsomega.5c11459.pdf by guest on 24 November 2026

https://doi.org/10.1021/acsomega.5c11459
ACS Omega 2026, 11, 26411−26420

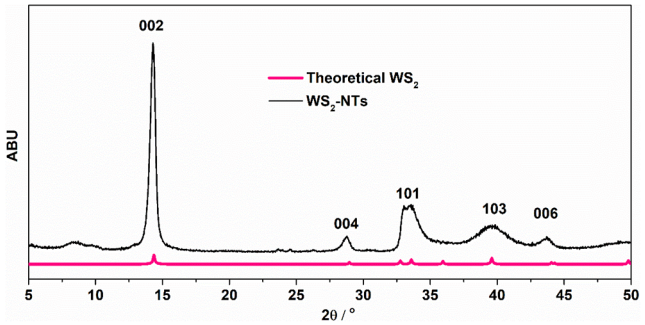

Figure 1. X-ray diffraction pattern of WS2 nanotubes.

Preparation of the Composite

Ten mg of WS_2 nanotubes (WS_2−NTs) were weighed in a glass vial, after which, 10 mL of the solvent mixture of dimethylformamide (DMF) and dimethyl sulfoxide (DMSO) (V(DMF)/V(DMSO) = 4:1) was added. The prepared suspension was sonicated in an ultrasonic bath for 2 h with intermittent mixing of the suspension.

The as-prepared suspension of DMF/DMSO with 1 mg mL^{-1} WS_2−NTs was used to prepare diluted suspensions of the same DMF/DMSO mixtures. These suspensions were used as solvents for the preparation of the 1.4 mol dm^{-3} $Cs_{0.1}FA_{0.9}PbI_{2.9}Br_{0.1}$ precursor solution. These solutions were spin-coated on glass substrates at 4000 rpm with the addition of chlorobenzene as the antisolvent to prepare thin films with an average thickness of 550 nm. The films were annealed on a hot plate at 150 °C for 10 min for the PVSK to crystallize in the cubic perovskite lattice.

Characterization

The TEM measurements of WS_2−NTs were performed by JEOL 2100F, an instrument operating at 200 kV. The scanning electron micrograph (SEM) of WS_2−NTs was recorded by a scanning electron microscope: LEO model Supra, 7426. The SEM of the composite was recorded with a field-emission SEM, model JSM-7000F, manufactured by JEOL Ltd. (Tokyo, Japan), using an accelerating voltage of 10 kV. Dynamic light scattering (DLS) measurements were carried out using a photon correlation spectrophotometer equipped with a 532 nm laser (Zetasizer Nano ZS, Malvern Instruments, Worcestershire, U.K.), at a backscattering angle of 173°, and the hydrodynamic diameter (d_h) was determined from the maximum of the volume-based size distribution to minimize the contribution of larger particles to the measured signal. Each sample was measured six times, and representative results are reported. Data analysis was conducted using Zetasizer Software version 7.13 (Malvern Instruments, Worcestershire, U.K.). All measurements were performed at a controlled temperature of 25.0 °C. Measurements were conducted over four h to monitor potential changes in dispersion stability. The profilometry was measured on the contact profilometer AlphaStep D600 (California, USA). The XRD of the WS_2 NTs was recorded by Ultima III (Rigaku, Japan) operating at 40 kV and 40 mA and using Cu Kα radiation (0.154 18 nm), while Empyrian, Malvern Panalytical (United Kingdom), operating at 40 kV and 40 mA and using Cu Kα radiation was used to record the composite. The optical properties were studied by UV−vis spectroscopy using an Ocean Optics HR4000 spectrometer (Ocean Optics, Largo, FL, USA) equipped with an integration sphere and a Xe 150-W light source. Atomic force microscopy (AFM) topography images were acquired in atmospheric conditions in the dark for PVSK thin films on ITO substrates using JPK NanoWizard 4 AFM Ultraspeed in contact mode. The conductive diamond AFM probes were obtained from Bruker (DDESP-V2 with a radius of curvature of 100 nm, a nominal spring constant of 80 N/m, and a nominal resonant frequency of 450 kHz). Surface conductivity was acquired in c-AFM mode by applying a bias voltage of 2 V to the sample and measuring current between tip and sample. Samples were kept in the dark during the measurements. All images were processed by using JPK Data processing. The electrical conductivity of the prepared PVSK thin films on the ITO-patterned glass substrate was measured by impedance spectroscopy (Novocontrol α-A Dielectric Spectrometer, Novocontrol Technologies, Montabaur, Germany) in the frequency range from 0.1 Hz to 1 MHz at 20 mV. All of the measurements were performed at room temperature. Gold electrodes were evaporated onto the PVSK film (top contact), and the ITO glass substrate (bottom contact) served as electrical contacts. Such an electrode configuration enabled the electrical characterization of the film in the cross-sectional geometry, see Supporting Figure S1. To check the homogeneity of the thin films, the measurements were performed multiple times (each time on a different 9 mm^2 sample area) under identical experimental conditions. The photoconductivity measurements were performed under illumination of the AM1.5 solar spectrum with an irradiance of 100 mW cm^{-2}, calibrated using a Sciencetech Inc. Sun reference solar cell, in the ambient atmosphere using the same contact setup.

RESULTS AND DISCUSSION

WS_2−NT Characterization

The micrographs in Figure 2 confirm that the synthesized WS_2 nanotubes are under 100 nm in thickness, with a length on the micron scale. The TEM image (Figure 2b) shows that the nanotube mantle is clearly monocrystalline, which is of importance for their electrical properties.[38] It is clear that the samples are tubes with hollow cores. The difference in the apparent orientation of the nanotubes when looking at the edge in contrast to the middle part is due to the curvature of the tubes as the edges of the nanotubes also exhibit a clear monocrystalline orientation.

Morphology

SEM images (Figure 3) show that the inclusion of WS_2 nanotubes, prepared using the method described here, did not significantly influence the grain size of the prepared perovskite films. In a similar system, others have reported the

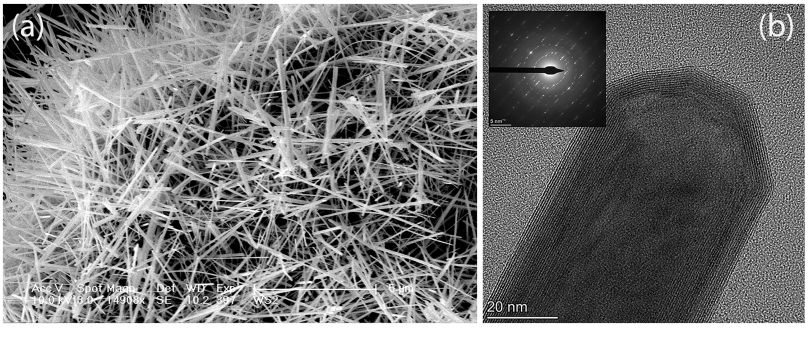

Figure 2. (a) SEM and (b) TEM images of synthesized WS2 nanotubes. Selected-area electron diffraction (SAED) is shown as an inset

Downloaded from pubs.acs.org/acsodf/article-pdf/11/18/26411/6614355/4/acsomega.5c11459.pdf by guest on 24 November 2026

https://doi.org/10.1021/acsomega.5c11459
ACS Omega 2026, 11, 26411−26420

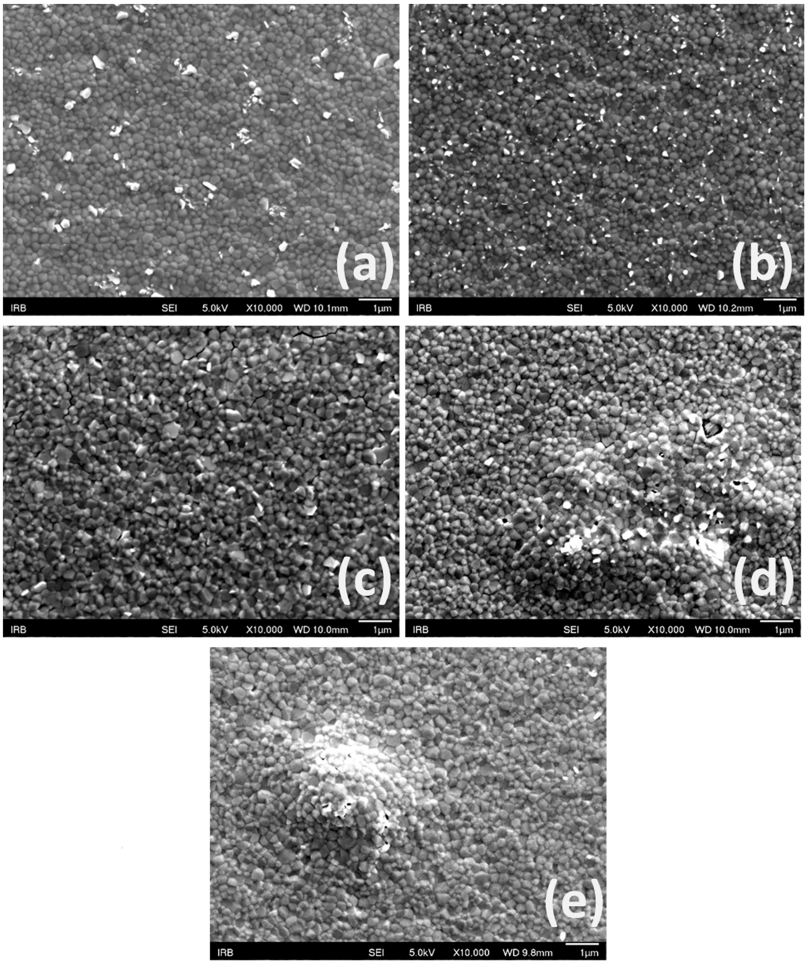

Figure 3. SEM images of (a) pure PVSK and PVSK with (b) 0.01, (c) 0.1, (d) 0.5, and (e) 1 mg mL^{-1} WS_2−NT.

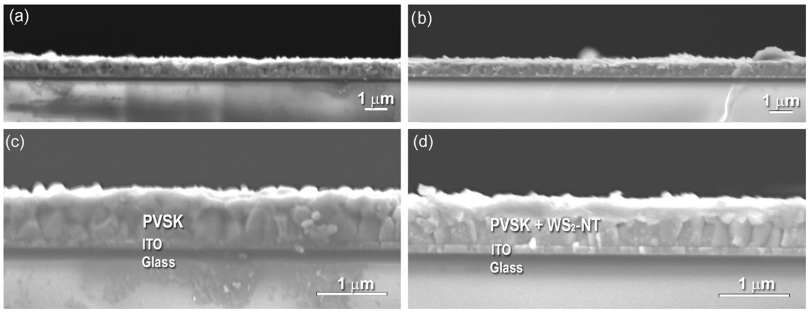

Figure 4. SEM cross-section images with 5.000 times magnification of (a) pure perovskite thin films (PVSK), (b) perovskite thin films with 0,1 mg mL^{-1} WS_2 nanotubes (PVSK+ WS_2−NT), and 15.000 times magnification of (c) PVSK, (d) PVSK+ WS_2−NT.

formation of larger grains of $MAPbI_3$ perovskite with the inclusion of WS_2 nanoparticles.[44] We argue that the inclusion of WS_2 nanotubes, which have one dimension on the nanoscale and with their length being far larger than the nanoscale, did not encourage any Ostwald ripening during the crystal growth of the perovskite grains. The number of white dots (which are most likely PbI_2 crystals) in the SEM images is also lower near the WS_2 nanotubes. SEM cross-section images of pure perovskite and perovskite with 0.1 mg mL^{-1} WS_2−NTs under lower magnification (Figure 4a,b) show homogeneous layer thickness. Moreover, the addition of WS_2 nanotubes in perovskite did not influence crystal grain quality in terms of their respective shape and size (Figure 4c,d). In both cases, perovskite crystal grains show a uniform, lateral shape with little to no grain boundaries from the bottom to the top of the film. This is crucial for efficient perovskite solar devices, as grain boundaries are defect-rich and show significantly lower conductivity. When grain boundaries are present laterally through the film, they obstruct the electron path, ultimately lowering solar cell efficiency.[48] Furthermore, this indicates a higher thin-film stability. In cases where grain boundaries are present laterally through the film, significant charge accumulation occurs, leading to a more rapid degradation. Perovskites' low conductivity can result in charge accumulation, especially on grain boundaries exposed to the ambient environment, which can drive the perovskite degradation mechanism.[49] An

Downloaded from pubs.acs.org/acsodf/article-pdf/11/18/26411/6614354/acsomega.5c11459.pdf by guest on 24 November 2026

https://doi.org/10.1021/acsomega.5c11459
ACS Omega 2026, 11, 26411−26420

Table 1. Hydrodynamic Diameter (d_h) and Volume Distribution (Vol. %) of 0.1 and 0.01 mg mL^{-1} WS_2 Nanotubes Suspended in DMF/DMSO Solution during Four Hours at 25 Degrees Celsius

concentration	0.1 mg mL^{-1}					
t/h	d_h distribution 1/nm	vol. %	d_h distribution 2/nm	vol. %	d_h distribution 3/nm	vol. %
0	73.0 ± 3.2	1.5 ± 0.1	371.6 ± 21.1	84.1 ± 2.9	5440.8 ± 60.4	12.3 ± 3.7
1			456.2 ± 89.9	86.9 ± 5.3	5280.0 ± 162.6	11.5 ± 3.7
2			403.4 ± 56.7	86.1 ± 3.0	5374. ± 75.3	13.3 ± 3.1
3			378.8 ± 32.1	90.0 ± 6.4	5459.6 ± 36.7	9.0 ± 1.8
4			400.5 ± 29.3	87.2 ± 3.2	5365.5 ± 105.8	10.8 ± 4.5
concentration	0.01 mg mL^{-1}					
t/h	d_h distribution 1/nm	vol. %	d_h distribution 2/nm	vol. %	d_h distribution 3	vol. %
0	347.2 ± 24.9	92.2 ± 8.9	5437.3 ± 64.9	7.9 ± 3.4		
1	370.8 ± 35.1	91.9 ± 4.9	5516.0 ± 49.6	9.4 ± 3.3		
2	387.0 ± 30.0	90.5 ± 3.5	5515.5 ± 77.4	8.0 ± 3.5		
3	370.4 ± 25.4	88.4 ± 7.0	5433.6 ± 95.3	13.9 ± 4.6		
4	418.0 ± 51.6	90.8 ± 4.8	5467.0 ± 42.8	7.8 ± 3.0		

increase in conductivity, which in this case can be the consequence of WS_2 particles, can mitigate this effect. In the case of the film prepared from the perovskite precursor solution containing WS_2−NTs at a concentration of 0.1 mg mL^{-1}, a noticeable change can be observed where the grains display a less rounded, more faceted cuboidal structure, accompanied by the presence of several larger grains, while at higher concentrations (0.5 and 1 mg mL^{-1}) we can observe the formation of mounds on the film surface, corresponding to the formation of WS_2−NTs aggregates in the perovskite film (Figure S2). We can then conclude that the WS_2−NTs were evenly dispersed throughout the perovskite film, horizontal to the substrate, and with no obvious protrusion from the surface when the concentration was below 0.5 mg mL^{-1}. On the other hand, it can be expected that at larger concentrations of the nanotubes form a mesoscopic framework inside the perovskite thin film, given the dimensions of the nanotubes (1 μm or larger in their length) and the thickness of the perovskite thin films of 500−700 nm (Supporting Table S1). It is also worth pointing out that by increasing the amount of WS_2−NTs in the PVSK film, the thickness of the film gradually increases. Given the obtained morphology, the focus of the film analysis was oriented to the 0.1 mg mL^{-1} WS_2−NT concentration as it lies in the optimal zone of having the highest WS_2−NT concentration without an impact on the film's morphology.

To confirm that the chosen WS_2−NT concentration was suitable for further film investigation, the colloidal stability of nanotubes in the DMF/DMSO (4:1) solvent system was investigated by performing dynamic light scattering (DLS) measurements. The stability of WS_2−NTs in the solvent was measured at two different concentrations over 4 h. The chosen concentrations of 0.1 and 0.01 mg mL^{-1} were used to assess whether the lower concentration is more suitable (Table 1). DLS measurements showed that both concentrations are stable for 4 h. The dominant population is around 400 nm, with a smaller secondary population at approximately 5000 nm. The results indicate that WS_2−NTs aggregate in solution but are stable over time, meaning these suspensions are suitable for use. The more dilute sample (0.01 mg mL^{-1}) exhibited a marginal reduction in the volume percentage of large aggregates, but overall, the size distribution remained similar to that at 0.1 mg mL^{-1}. This indicates that dilution has a minimal impact on dispersibility or stability within this concentration range.

Additionally, we have evaluated with DLS if the WS_2−NTs inside the suspension break during sonication (Table 2).

Table 2. Hydrodynamic Radius (d_h) and Volume Distribution (Vol. %) of 0.1 and 0.01 mg mL^{-1} WS_2 Nanotubes Suspended in DMF/DMSO Solution before and after Sonification at 25 Degrees Celsius

concentration	before sonification/nm	after sonification/nm
0.1 mg mL^{-1}	177.9 ± 105.0 (vol. % 80.6 ± 43.3)	77.6 ± 13.9 (vol. % 3.1 ± 0.5) 377.0 ± 38.1 (vol. % 85.8 ± 2.4) 5398.3 ± 70.4 (vol. % 11.1 ± 2.0)
0.01 mg mL^{-1}	318.0 ± 163.6 (vol. % 100)	85.3 ± 7.4 (vol. % 1.4 ± 1.3) 338.3 ± 33.3 (vol. % 90.3 ± 4.7) 5465.5 ± 62.8 (vol. % 8.3 ± 2.1)

Before sonication, the suspensions appeared highly aggregated with poorly defined or unstable size distributions, especially at 0.1 mg mL^{-1}. Due to the precipitation of these large aggregates at the bottom of the measuring vial, DLS measures only sporadic particles or aggregates formed above the sediment. Before sonication, only one distribution is observed, with a broad size range and an average size of 177.9 ± 105 nm. In contrast, sonication results in a more dispersed suspension. Three distributions are observed, with the most dominant being 377.0 ± 38.1 nm (vol. % 85.8 ± 2.4). Larger aggregates are also detected, with a size of 5398.4 ± 70.4 nm (vol. % 11.1 ± 2.0). But, the third detected distribution is 77.6 ± 13.9 nm, present at a very small vol. % of 3.1 ± 0.5. These findings indicate that sonication significantly improves the dispersion of WS_2−NTs but can also cause partial fragmentation of the WS_2−NTs.

Structure

The role of WS_2−NTs is to affect the charge mobility in the perovskite composite thin film while preserving the crystal structure of the PVSK material. Therefore, it is important for the PVSK films to remain in the cubic photoactive phase, as adding different components may impact the integrity of its crystal structure or the cubic phase's formation of the thin film.[50] The XRD patterns of the pure PVSK film and PVSK with 0.1 mg mL^{-1} WS_2−NT are shown in Figure 4.

As shown in Figure 5, the inclusion of WS_2−NTs with a concentration of 0.1 mg mL^{-1} does not alter the crystallinity of the PVSK FA-based thin film nor promote the formation of the hexagonal delta perovskite phase. The peaks of WS_2 are not

Downloaded from pubs.acs.org/acsodf/article-pdf/11/18/26411/6614354/acsomega.5c11459.pdf by guest on 24 November 2026

https://doi.org/10.1021/acsomega.5c11459
ACS Omega 2026, 11, 26411−26420

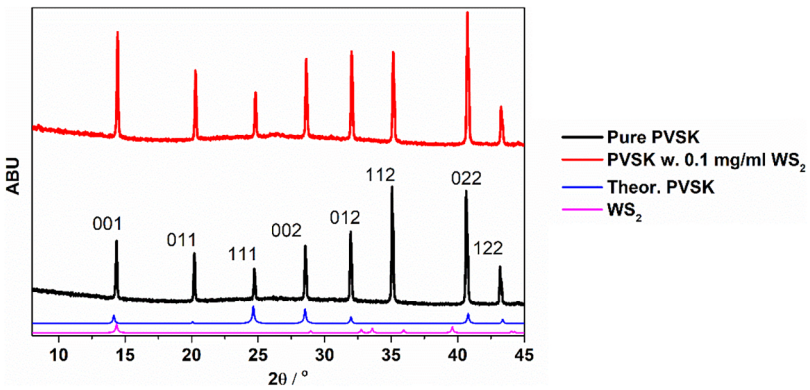

Figure 5. XRD pattern of pure PVSK and PVSK with 0.1 mg mL^{-1} WS_2−NT together with theoretical XRD patterns of PVSK and WS_2.

visible on the XRD patterns, which is due to the small concentration of the WS_2−NTs in the thin film compared to the PVSK. If we were to recalculate the molar PVSK concentration of 1.4 mol dm^{-3} to the mass concentration, we would obtain a value of 891.9 mg mL^{-1}. In other words, the ratio PVSK: WS_2−NTs was almost 4 orders of magnitude and the lack of WS_2−NTs diffraction patterns in this measurement was expected. The (112) plane of the experimentally obtained PVSK appears as a result of the polycrystalline nature of the thin film (in which many crystal orientations are present, as shown in Supporting Figure S3), as theoretical patterns are derived from monocrystals in which the plane is not preferred.

Optical Measurements

Optical measurements of the perovskite thin films are listed in Figure 6.

Figure 6 shows that the optical properties, e.g., the transmittance, are not impacted by the inclusion of the mesoframework of the WS_2−NT throughout the various concentrations. All of the films show a steep drop in the transmittance of the visible part of the spectrum around the wavelength of 800 nm (Figure 6a). The resonance reflection of the incident light between the optical medium of the substrate and the thin films (PVSK thin film, ITO thin film, and the glass substrate) can be seen at wavelengths above 800 nm. In the spectral region above the perovskite band gap (above 800 nm), the transmittance variations between samples are relatively large compared with those in the sub-band gap region. The decrease in transmittance at the visible interference maxima for each sample can be attributed to the combined effect of increased film thickness and higher WS_2−NT content in the perovskite layer. In the sub-band gap region, the perovskite layer already exhibits a very high absorption coefficient, so the additional influence of WS_2 nanotubes is expected to be minor, and the sample-to-sample variation in transmittance is on the order of only 2−3%. For the observed transmittance drop, the optical band gaps were calculated using a Tauc plot. For the pure PVSK film and the film with 0.1 mg mL^{-1} WS_2−NT, band gaps of 1.55 and 1.57 eV were obtained, respectively (Figure 6b). This difference in the optical gap, alongside the visual variation of the transmittance curves, was likely a systemic error in the sample measurement rather than the effect of WS_2−NTs.

Electrical Measurements

Electrical measurements of the pure PVSK and PVSK containing 0.01−1 mg mL^{-1} WS_2−NT were performed by IS. The best result was obtained for the sample containing 0.1

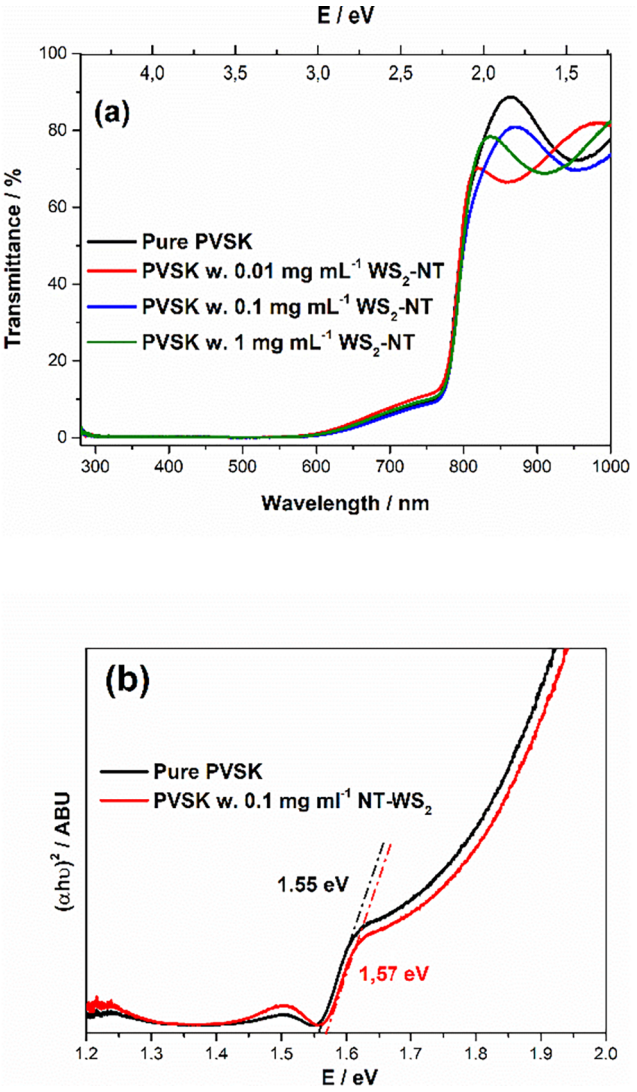

Figure 6. (a) Optical transmittance measurements of pure PVSK and PVSK with 0.1 and 0.01 mg mL^{-1} WS_2−NTs; (b) Tauc plot for the PVSK and PVSK with 0.1 mg mL^{-1} WS_2−NT.

mg mL^{-1} WS_2−NT (Figure 7). The samples with WS_2−NTs concentrations of 0.05 and 0.01 mg mL^{-1} showed similar results to those of the pure PVSK. On the other hand, samples with ≥0.5 mg mL^{-1} WS_2−NTs exhibited high morphological heterogeneity due the aggregation of NTs (Figure 3); hence,

Downloaded from pubs.acs.org/acsodf/article-pdf/11/18/26411/6614355/acsomega.5c11459.pdf by guest on 24 November 2026

https://doi.org/10.1021/acsomega.5c11459
ACS Omega 2026, 11, 26411−26420

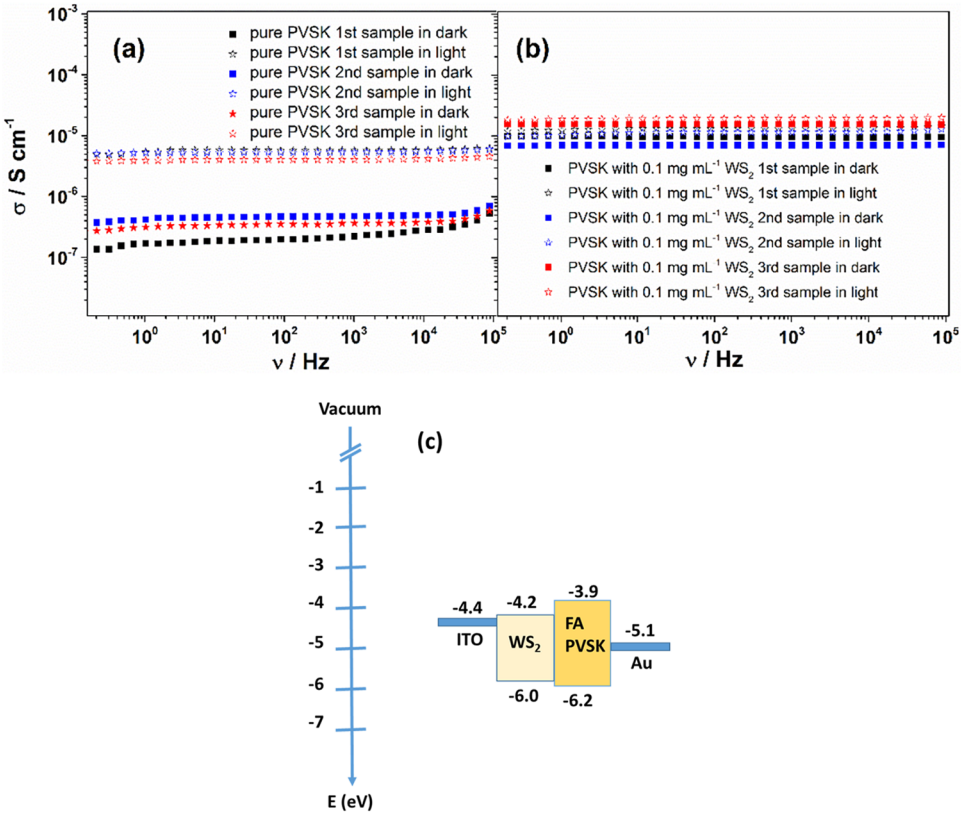

Figure 7. Conductivity spectra of (a) pure PVSK and (b) PVSK with 0.1 mg mL^{-1} WS_2−NT, repeated on multiple samples for reproducibility; (c) energy-level diagrams of WS_2 and PVSK[51,52] heterojunction.

their electrical measurements were not consistent and were not considered for detailed electrical characterization.

The results obtained for the pure PVSK thin films are comparable to our previously published results,[46] where we showed that the conductivity of a pure FAPI thin film ranges from 5×10^{-6} to 1×10^{-7} S cm^{-1} in the dark. When illuminated, the conductivity increases approximately 1.5 orders of magnitude, which is also in a good agreement with our previous study.[53] This increase can be attributed to an increase in the concentration of the charge carriers in the conduction band of the semiconducting material. The electrical conductivity can be formulated as a function of mobility, given by the following equation

$$\sigma = en\mu_e + ep\mu_h \quad (1)$$

where σ is the electrical conductivity, e is the electric charge of the electron, n and p are the concentrations of electrons and holes and μ_e and μ_h are the mobilities of electrons and holes, respectively. Under illumination, the concentration of electrons and holes increases due to the formation of photogenerated charge carriers, which leads to a rise in the conductivity of the material. Interestingly, when the WS_2−NTs are introduced into the PVSK matrix, the conductivity measured in the dark is around 2 orders of magnitude higher than for the pure PVSK ($\sigma \approx 2.5 \times 10^{-5}$ S cm^{-1}), but increases only slightly (roughly 2 times) under light (Figure 7b). Overall, the conductivity of the PVSK with 0.1 mg mL^{-1} WS_2−NTs in the dark and in the light is higher than that of pure PVSK under the same conditions, comparing Figure 7a,b. Conductivity enhancement was further investigated by conductive AFM measurements performed in the dark (Figure S4) to validate the observed changes in the electrical properties of the PVSK thin film. Average surface conductivity was determined by analyzing histograms of a raw c-AFM data measured on three different regions of the samples. The average current measured for pristine PVSK was 41.8 ± 1.1 pA, whereas the incorporation of WS_2−NTs increased this value to 114 ± 1.0 pA, corresponding to an approximate 2.5-fold enhancement. It is important to note that although IS measures conductivity and conductive AFM measures electrical current, both parameters originate from the intrinsic electrical properties of the material. Consequently, modifications in charge transport mechanisms can influence both the material's resistance (which depends on the measured current) and its conductivity. One plausible explanation for the observed enhancement in these heterogeneous semiconducting systems is the interfacial contact between PVSK and WS_2, which facilitates charge separation (Figure 7c). Conductivity increase was not observed on thin films with 1 and 0.01 mg mL^{-1} WS_2−NTs (Figure S5). For 1 mg mL^{-1}, formed films display poorer conductivity when compared to pristine films (especially under illumination), which is to be expected from films with poor morphology and aggregated nanotubes that induce film defects. On the other hand, films with 0.01 mg mL^{-1} concentration contain insufficient nanotubes for any measurable effect to be observed. These observations further support the findings in the concentration range of 0.1 mg mL^{-1} WS_2−NTs.

The monocrystalline nature of WS_2−NTs, as well as WS_2 closed-cage conductivity, is likely the cause of the increased conductivity of the material. This can be seen in the dark conductivity rise of the PVSK/WS_2−NT films, since the concentration of the charge carriers remained the same, then

Downloaded from pubs.acs.org/acsodf/article-pdf/11/18/26411/6614355/acsomega.5c11459.pdf by guest on 24 November 2026

https://doi.org/10.1021/acsomega.5c11459
ACS Omega 2026, 11, 26411−26420

the mobility must have changed, given eq 1. When illuminated, the observed small increase in conductivity can be explained by the small increase in the charge-carrier concentration via the photogenerated species. We hypothesize that the increase in the carrier concentration is smaller than the change in the carrier mobility in the PVSK/WS_2−NT films. In other words, conductivity is influenced to a lesser extent by the presence of photogenerated charge carriers than by the increase in carrier mobility, which explains the comparatively small conductivity enhancement observed under illumination This effect does not appear at lower concentrations of WS_2−NTs, nor is it present when the WS_2−NTs aggregate inside the perovskite thin film. At very low concentrations, the amount of WS_2−NTs is insufficient to influence the charge transport, while at higher concentrations, the aggregation reduces the film homogeneity and impacts the reproducibility of the electrical response. Nevertheless, the observed increase in conductivity of the PVSK with 0.1 mg mL^{-1} WS_2−NTs under illumination suggests that WS_2−NTs can extend the transport pathways of photogenerated species due to their intrinsic conductivity. In assembled solar cells, such behavior could manifest itself as an increased short-circuit current density (J_{sc}), a lower series resistance, and ultimately a higher efficiency when compared to that of pure perovskite films. As the IS setup was set up in an ambient atmosphere, the exposure to air moisture and oxygen leads to degradation of the perovskite thin films and electrical measurements become irregular when repeated after an average of 7 days. The observed degradation rates were practically identical for pure PVSK and PVSK modified with WS_2−NTs.

CONCLUSION

We successfully prepared $Cs_{0.1}FA_{0.9}PbI_{2.9}Br_{0.1}$ perovskite thin films by incorporating WS_2 nanotubes inside the thin film. The inclusion of nanotubes in a small concentration did not impact on the morphology of the thin film, while at higher concentrations the agglomeration of the nanotubes was pronounced. While optical measurements were similar throughout the range of WS_2-nanotube concentrations, IS showed that under certain concentrations (optimally at 0.1 mg mL^{-1}) the inclusion of WS_2 nanotubes positively impacted the conductivity of the thin film by facilitating the charge transfer from the perovskite to the nanotube material. These results show promise for perovskite/WS_2−NT composite thin films and their application in future optoelectronic research.

ASSOCIATED CONTENT

Supporting Information

The Supporting Information is available free of charge at https://pubs.acs.org/doi/10.1021/acsomega.5c11459.

Additional experimental data and methods, including photographs of the experimental setup (PDF)

AUTHOR INFORMATION

Corresponding Author

Vedran Kojić − *Institute Ruđer Bošković, Divison of Materials Physics, 10000 Zagreb, Croatia;* orcid.org/0009-0009-1165-9090; Email: vkojic@irb.hr

Authors

Stjepan Dolić − *Institute Ruđer Bošković, Divison of Materials Physics, 10000 Zagreb, Croatia; Faculty of Science, Department of Chemistry, 10000 Zagreb, Croatia*

Alla Zak − *Physics Department, the Faculty of Sciences, Holon Institute of Technology, 5810201 Holon, Israel;* orcid.org/0000-0002-3807-3454

Alex Laikhtman − *Physics Department, the Faculty of Sciences, Holon Institute of Technology, 5810201 Holon, Israel;* orcid.org/0000-0003-1603-286X

Hongbo Mo − *Department of Physics, University of Hong Kong, Kowloon, Hong Kong 999077, China*

Tihana Čižmar − *Institute Ruđer Bošković, Divison of Materials Physics, 10000 Zagreb, Croatia*

Ina Erceg − *Institute Ruđer Bošković, Divison of Materials Physics, 10000 Zagreb, Croatia*

Lucija Klobučar − *Institute Ruđer Bošković, Divison of Materials Physics, 10000 Zagreb, Croatia; Faculty of Science, Department of Chemistry, 10000 Zagreb, Croatia*

Iva Šrut Rakić − *Institute of Physics, Center for Advanced Laser Techniques, 10000 Zagreb, Croatia;* orcid.org/0000-0001-5184-8130

Krunoslav Juraić − *Institute Ruđer Bošković, Divison of Materials Physics, 10000 Zagreb, Croatia*

Andreja Gajović − *Institute Ruđer Bošković, Divison of Materials Physics, 10000 Zagreb, Croatia;* orcid.org/0000-0002-5488-2227

Complete contact information is available at: https://pubs.acs.org/10.1021/acsomega.5c11459

Notes

The authors declare no competing financial interest.

ACKNOWLEDGMENTS

Authors would like to acknowledge Ana Šantić for providing the insight in the solid state impedance spectroscopy theory, Aleksandra B. Djurišić for editing the writing style of the paper and Paul McGuiness for English language editing. The presented results were obtained within the framework of cooperation between the Government of the Republic of Croatia and the Government of the State of Israel with cofinancing from the Ministry of Science, Education and Youth Croatia and the Ministry of Science and Technology of Israel, project Novel perovskite solar cells with enhanced performance based on hybrid halide perovskite/transition-metal disulfides nanocomposites (Sol-HP-TMD-NanoComp). The authors acknowledge partial financial support from the European Regional Development Fund for the project "Materials for clean energy, advanced sensors and quantum technologies" (Grant No. PK.1.1.10.0002). This article is based on work from the STSM grant (A.L.) of the COST Action RenewPV CA21148, supported by COST (European Cooperation in Science and Technology).

REFERENCES

(1) Akkerman, Q. A.; Manna, L. What Defines a Halide Perovskite? *ACS Energy Lett.* **2020**, *5* (2), 604−610.

(2) Garba, Z. N.; Zhou, W.; Zhang, M.; Yuan, Z. A review on the preparation, characterization and potential application of perovskites as adsorbents for wastewater treatment. *Chemosphere* **2020**, *244*, No. 125474.

Downloaded from pubs.acs.org/acsodf/article-pdf/11/18/26411/6614354/acsomega.5c11459.pdf by guest on 24 November 2026

(3) Qiu, F.; Sun, J.; Zhang, Z.; Shen, T.; Liu, H.; Qi, J. Achieving stable and high-efficiency (>21%) lead halide perovskite solar cells with δ-$CsPbI_2Br$ seed−assisted growth strategy. *Mater. Today Energy* **2021**, *21*, No. 100837.
(4) Cho, H.; Jeong, S. H.; Park, M. H.; Kim, Y. H.; Wolf, C.; Lee, C. L.; Heo, J. H.; Sadhanala, A.; Myoung, N.; Yoo, S.; Im, S. H.; Friend, R. H.; Lee, T. W. Overcoming the electroluminescence efficiency limitations of perovskite light-emitting diodes. *Science* **2015**, *350*, 1222.
(5) Zhang, Q.; Shang, Q.; Su, R.; Do, T. T. H.; Xiong, Q. Halide Perovskite Semiconductor Lasers: Materials, Cavity Design, and Low Threshold. *Nano Lett.* **2021**, *21* (5), 1903−1914.
(6) Mai, H.; Chen, D.; Tachibana, Y.; Suzuki, H.; Abe, R.; Caruso, R. A. Developing sustainable, high-performance perovskites in photocatalysis: design strategies and applications. *Chem. Soc. Rev.* **2021**, *50*, 13692−13729.
(7) Zhao, J.; Zhao, L.; Deng, Y.; Xiao, X.; Ni, Z.; Xu, S.; Huang, J. Perovskite-filled membranes for flexible and large-area direct-conversion X-ray detector arrays. *Nat. Photonics* **2020**, *14*, 612−617.
(8) Hu, S.; Ren, Z.; Djurišić, A. B.; Rogach, A. L. Metal Halide Perovskites as Emerging Thermoelectric Materials. *ACS Energy Lett.* **2021**, *6* (11), 3882−3905.
(9) Wang, T.; Son, J. S. Progress and perspective of halide perovskites thermoelectrics: Balance between performance and stability. *APL Energy* **2025**, *3*, No. 021503.
(10) Green, M. A.; Dunlop, E. D.; Yoshita, M.; Kopidakis, N.; Bothe, K.; Siefer, G.; Hao, X.; Jiang, J. Y. Solar Cell Efficiency Tables (Version 66). *Prog. Photovolt.: Res. Appl.* **2025**, *33* (7), 795−810.
(11) Chen, B.-A.; Lin, J.-T.; Suen, N.-T.; Tsao, C.-W.; Chu, T.-C.; Hsu, Y.-Y.; Chan, T.-S.; Chan, Y.-T.; Yang, J.-S.; Chiu, C.-W.; Chen, H. M. In Situ Identification of Photo- and Moisture-Dependent Phase Evolution of Perovskite Solar Cells. *ACS Energy Lett.* **2017**, *2* (2), 342−348.
(12) Leguy, A. M. A.; Hu, Y.; Campoy-Quiles, M.; Alonso, M. I.; Weber, O. J.; Azarhoosh, P.; van Schilfgaarde, M.; Weller, M. T.; Bein, T.; Nelson, J.; Docampo, P.; Barnes, P. R. F. Reversible Hydration of CH3NH3PbI3 in Films, Single Crystals, and Solar Cells. *Chem. Mater.* **2015**, *27* (9), 3397−3407.
(13) Aristidou, N.; Sanchez-Molina, I.; Chotchuangchutchaval, T.; Brown, M.; Martinez, L.; Rath, T.; Haque, S. A. The Role of Oxygen in the Degradation of Methylammonium Lead Trihalide Perovskite Photoactive Layers. *Angew. Chem., Int. Ed.* **2015**, *54* (28), 8208−8212.
(14) Hidalgo, J.; Kaiser, W.; An, Y.; Li, R.; Oh, Z.; Castro-Méndez, A.-F.; LaFollette, D. K.; Kim, S.; Lai, B.; Breternitz, J.; Schorr, S.; Perini, C. A. R.; Mosconi, E.; De Angelis, F.; Correa-Baena, J.-P. Synergistic Role of Water and Oxygen Leads to Degradation in Formamidinium-Based Halide Perovskites. *J. Am. Chem. Soc.* **2023**, *145* (45), 24549−24557.
(15) Ali, M. U.; Mo, H.; Rehman, A. U.; Leung, T. L.; Djurišić, A. B. Metal halide perovskites: stability under illumination and bias. *Trends Chem.* **2024**, *6* (5), 248−259.
(16) Chen, Z.; Yang, Z.; Du, S.; Lin, D.; Zhang, F.; Zeng, Y.; Liu, G.; Nie, Z.; Ma, L. Thermal stability and decomposition kinetics of mixed-cation halide perovskites. *Phys. Chem. Chem. Phys.* **2023**, *25*, 32966−32971.
(17) Leblebici, S. Y.; Leppert, L.; Li, Y.; Reyes-Lillo, S. E.; Wickenburg, S.; Wong, E.; Lee, J.; Melli, M.; Ziegler, D.; Angell, D. K.; Ogletree, D. F.; Ashby, P. D.; Toma, F. M.; Neaton, J. B.; Sharp, I. D.; Weber-Bargioni, A. Facet-dependent photovoltaic efficiency variations in single grains of hybrid halide perovskite. *Nat. Energy* **2016**, *1* (8), No. 16093.
(18) Zhou, Y.; Herz, L. M.; Jen, A. K.-Y.; Saliba, M. Advances and challenges in understanding the microscopic structure−property−performance relationship in perovskite solar cells. *Nat. Energy* **2022**, *7*, 794−807.
(19) Fujiwara, H.; Kato, M.; Tamakoshi, M.; Miyadera, T.; Chikamatsu, M. Optical Characteristics and Operational Principles of Hybrid Perovskite Solar Cells. *Phys. Status Solidi A* **2018**, *215* (12), No. 1700730.
(20) Tailor, N. K.; Abdi-Jalebi, M.; Gupta, V.; Hu, H.; Dar, M. I.; Li, G.; Satapathi, S. Recent progress in morphology optimization in perovskite solar cell. *J. Mater. Chem. A* **2020**, *8*, 21356−21386.
(21) Chen, L.-C.; Lee, K.-L.; Wu, W.-T.; Hsu, C.-F.; Tseng, Z.-L.; Sun, X. H.; Kao, Y.-T. Effect of Different $CH_3NH_3PbI_3$ Morphologies on Photovoltaic Properties of Perovskite Solar Cells. *Nanoscale Res. Lett.* **2018**, *13*, 140.
(22) Awais, M.; Gangadharan, D. T.; Tan, F.; Saidaminov, M. I. How to Make 20% Efficient Perovskite Solar Cells in Ambient Air and Encapsulate Them for 500 h of Operational Stability. *Chem. Mater.* **2022**, *34* (18), 8112−8118.
(23) Saliba, M.; Correa-Baena, J.-P.; Wolff, C. M.; Stolterfoht, M.; Phung, N.; Albrecht, S.; Neher, D.; Abate, A. How to Make over 20% Efficient Perovskite Solar Cells in Regular (*n*−*i*−*p*) and Inverted (*p*−*i*−*n*) Architectures. *Chem. Mater.* **2018**, *30* (13), 4193−4201.
(24) Male, J. C. Hall effect measurement in semiconducting chalcogenide glasses and liquids. *Br. J. Appl. Phys.* **1967**, *18*, No. 1543.
(25) Dacuña, J.; Salleo, A. Modeling space-charge-limited currents in organic semiconductors: Extracting trap density and mobility. *Phys. Rev. B* **2011**, *84*, No. 195209.
(26) Arif, M.; Yun, M.; Gangopadhyay, S.; Ghosh, K.; Fadiga, L.; Galbrecht, F.; Scherf, U.; Guha, S. Polyfluorene as a model system for space-charge-limited conduction. *Phys. Rev. B* **2007**, *75*, No. 195202.
(27) Schauer, F.; Novotny, R.; Nešpůrek, S. Space-charge-limited-current spectroscopy: Possibilities and limitations. *J. Appl. Phys.* **1997**, *81*, No. 1244.
(28) Pitarch-Tena, D.; Ngo, T. T.; Vallés-Pelarda, M.; Pauporté, T.; Mora-Seró, I. Impedance Spectroscopy Measurements in Perovskite Solar Cells: Device Stability and Noise Reduction. *ACS Energy Lett.* **2018**, *3* (4), 1044−1048.
(29) Torres, J.; Zarazua, I.; Esparza, D.; Rivas, J. M.; Saliba, M.; Mora-Seró, I.; Turren-Cruz, S.-H.; Abate, A. Degradation Analysis of Triple-Cation Perovskite Solar Cells by Electrochemical Impedance Spectroscopy. *ACS Appl. Energy Mater.* **2022**, *5* (10), 12545−12552.
(30) Zheng, D.; Zhu, T.; Pauporté, T. Using Monovalent- to Trivalent-Cation Hybrid Perovskites for Producing High-Efficiency Solar Cells: Electrical Response, Impedance, and Stability. *ACS Appl. Energy Mater.* **2020**, *3* (11), 10349−10361.
(31) Haque, M. A.; Yu, T.; Choubisa, H.; Hernandez, L. H.; Zhou, Y.; Genovese, A.; Davaasuren, B.; Combe, C.; Li, H.; Luther, J. M.; Blackburn, J. L.; Sargent, E. H.; Ong, W.-L.; Baran, D. D. Nanoscale Decoupling of Carrier−Phonon Transport in Carbon Nanotube−Halide Perovskite Heterostructures. *Adv. Sci.* **2025**, *12* (43), No. e07589.
(32) Bansal, P.; Zhang, X.; Wang, H.; Kar, P.; Yu, W. W. Charge transfer between lead halide perovskite nanocrystals and single-walled carbon nanotubes. *Nanoscale Adv.* **2020**, *2*, 808−813.
(33) Zheng, D.; Schwob, C.; Prado, Y.; Ouzit, Z.; Coolen, L.; Pauporté, T. How do gold nanoparticles boost the performance of perovskite solar cells? *Nano Energy* **2022**, *94*, No. 106934.
(34) Haque, M. A.; Zhu, T.; Tounesi, R.; Lee, S.; Vafaie, M.; Huerta Hernandez, L.; Davaasuren, B.; Genovese, A.; Sargent, E. H.; Baran, D. Electrical Tunability of Quantum-Dot-in-Perovskite Solids. *ACS Nano* **2024**, *18* (50), 34089−34095.
(35) Wang, Q. H.; Kalantar-Zadeh, K.; Kis, A.; Coleman, J. N.; Strano, M. S. Electronics and optoelectronics of two-dimensional transition metal dichalcogenides. *Nat. Nanotechnol.* **2012**, *7*, 699−712.
(36) Sedova, A.; Višić, B.; Vega-Mayoral, V.; Vella, D.; Gadermaier, C.; Dodiuk, H.; Kenig, S.; Tenne, R.; Gvishi, R.; Bar, G. Silica aerogels as hosting matrices for WS2 nanotubes and their optical characterization. *J. Mater. Sci.* **2020**, *55*, 7612−7623.
(37) Sinha, S. S.; Višić, B.; Byregowda, A.; Yadgarov, L. Dynamical Nature of Exciton-Polariton Coupling in WS2 Nanoparticles. *Isr. J. Chem.* **2022**, *62*, No. e2021001.
(38) Ovchinnikov, D.; Allain, A.; Huang, Y.-S.; Dumcenco, D.; Kis, A. Electrical Transport Properties of Single-Layer WS_2. *ACS Nano* **2014**, *8*, 8174−8181.
(39) Zhang, Y.; Ye, J.; Matsuhashi, Y.; Iwasa, Y. Ambipolar MoS_2 Thin Flake Transistors. *Nano Lett.* **2012**, *12*, 1136−1140.

Downloaded from pubs.acs.org/acsodf/article-pdf/11/18/26411/6614355/acsomega.5c11459.pdf by guest on 24 November 2026

https://doi.org/10.1021/acsomega.5c11459
ACS Omega 2026, 11, 26411−26420

(40) Radisavljevic, B.; Radenovic, A.; Brivio, J.; Giacometti, V.; Kis, A. Single-layer MoS_2 transistors. *Nat. Nanotechnol.* **2011**, *6*, 147−150.
(41) Nik, Y. R.; Reyhani, A.; Farjami-Shayesteh, S.; Mortazavi, S. Z.; Taherkhani, A.; Aghaei, M. High-performance $CsGeBr_3$ perovskite/WS_2 Nano-Flakes Field-Effect Transistor at high temperature. *Opt. Mater.* **2022**, *132*, No. 112757.
(42) Wang, Q.; Wee, A. T. S. Upconversion Photovoltaic Effect of WS_2/2D Perovskite Heterostructures by Two-Photon Absorption. *ACS Nano* **2021**, *15* (6), 10437−10443.
(43) Zhang, D.-D.; Yu, R.-M. Perovskite-WS_2 Nanosheet Composite Optical Absorbers on Graphene as High-Performance Photo-transistors. *Front. Chem.* **2019**, *7*, No. 257.
(44) Immanuel, P. N.; Huang, S.-J.; Danchuk, V.; Sedova, A.; Prilusky, J.; Goldreich, A.; Shalom, H.; Musin, A.; Yadgarov, L. Improving the Stability of Halide Perovskite Solar Cells Using Nanoparticles of Tungsten Disulfide. *Nanomaterials* **2022**, *12*, No. 4454.
(45) Saliba, M.; Matsui, T.; Seo, J.-Y.; Domanski, K.; Correa-Baena, J.-P.; Nazeeruddin, M. K.; Zakeeruddin, S. M.; Tress, W.; Abate, A.; Hagfeldt, A.; Grätzel, M. Cesium-containing triple cation perovskite solar cells: improved stability, reproducibility and high efficiency. *Energy Environ. Sci.* **2016**, *9* (6), 1989−1997.
(46) Chithaiah, P.; Ghosh, S.; Idelevich, A.; Rovinsky, L.; Livneh, T.; Zak, A. Solving the "MoS2 Nanotubes" Synthetic Enigma and Elucidating the Route for Their Catalyst-Free and Scalable Production. *ACS Nano* **2020**, *14*, 3004−3016.
(47) Feldman, Y.; Frey, G. L.; Homyonfer, M.; Lyakhovitskaya, V.; Margulis, L.; Cohen, H.; Hodes, G.; Hutchison, J. L.; Tenne, R. Bulk Synthesis of Inorganic Fullerene-like MS2 (M = Mo, W) from the Respective Trioxides and the Reaction Mechanism. *J. Am. Chem. Soc.* **1996**, *118*, 5362−5367.
(48) Chu, Z.; Yang, M.; Schulz, P.; Wu, D.; Ma, X.; Seifert, E.; Sun, L.; Li, X.; Zhu, K.; Lai, K. Impact of grain boundaries on efficiency and stability of organic-inorganic trihalide perovskites. *Nat. Commun.* **2017**, *8*, No. 2230.
(49) Ahn, N.; Kwak, K.; Jang, M. S.; Yoon, H.; Lee, B. Y.; Lee, J.-K.; Pikhitsa, P. V.; Byun, J.; Choi, M. Trapped charge-driven degradation of perovskite solar cells. *Nat. Commun.* **2016**, *7*, No. 13422.
(50) Jeon, N. J.; Noh, J. H.; Yang, W. S.; Kim, Y. C.; Ryu, S.; Seo, J.; Seok, S. I. Compositional engineering of perovskite materials for high-performance solar cells. *Nature* **2015**, *517*, 476.
(51) Tao, S.; Schmidt, I.; Brocks, G.; Jiang, J.; Tranca, I.; Meerholz, K.; Olthof, S. Absolute energy level positions in tin- and lead-based halide perovskites. *Nat. Commun.* **2019**, *10*, No. 2560.
(52) Albu-Yaron, A.; Sinha, S. S.; Tenne, R. Nanotubes from two-dimensional materials in contemporary energy research: historical and perspective outlook. *ACS Energy Lett.* **2020**, *5* (5), 1498−1511.
(53) Kojić, V.; Bohač, M.; Bafti, A.; Pavić, L.; Salamon, K.; Čižmar, T.; Gracin, D.; Juraić, K.; Leskovac, M.; Capan, I.; Gajović, A. Formamidinium Lead Iodide Perovskite Films with Polyvinylpyrrolidone Additive for Active Layer in Perovskite Solar Cells, Enhanced Stability and Electrical Conductivity. *Materials* **2021**, *14*, No. 4594.

Downloaded from pubs.acs.org/acsodf/article-pdf/11/18/26411/6614354/acsomega.5c11459.pdf by guest on 24 November 2026

https://doi.org/10.1021/acsomega.5c11459
ACS Omega 2026, 11, 26411−26420